ROYAL SOCIETY OPEN SCIENCE

rsos.royalsocietypublishing.org

Research

Cite this article: Adhikari P, Khaoulaf R, Ez-Zahraouy H, Ching W-Y. 2017 Complex interplay of interatomic bonding in a multi-component pyrophosphate crystal: $K_2Mg(H_2P_2O_7)_2{\cdot}2H_2O$. *R. Soc. open sci.* **4**: 170982.
http://dx.doi.org/10.1098/rsos.170982

Received: 26 July 2017
Accepted: 30 October 2017

Subject Category:
Chemistry

Subject Areas:
computational chemistry

Keywords:
interatomic bonding, electronic properties, pyrophosphates

Author for correspondence:
Wai-Yim Ching
e-mail: chingw@mail.umkc.edu

This article has been edited by the Royal Society of Chemistry, including the commissioning, peer review process and editorial aspects up to the point of acceptance.

Electronic supplementary material is available online at https://dx.doi.org/10.6084/m9.figshare.c.3937672.

ROYAL SOCIETY OF CHEMISTRY

THE ROYAL SOCIETY PUBLISHING

Complex interplay of interatomic bonding in a multi-component pyrophosphate crystal: $K_2Mg(H_2P_2O_7)_2{\cdot}2H_2O$

Puja Adhikari[1], Redouane Khaoulaf[2,3], Hamid Ez-Zahraouy[3] and Wai-Yim Ching[1]

[1]Department of Physics and Astronomy, University of Missouri Kansas City, Kansas City, MO 64110, USA
[2]Department of Physics, Laboratory of Optoelectronics and Physical Chemistry of Materials, Faculty of Sciences, University Ibn Tofail, Kenitra, Morocco
[3]Laboratory of Condensed Matter and Interdisciplinary Sciences (LAMCSCI), Faculty of Sciences, University Mohammed V, Rabat, Morocco

W-YC, 0000-0001-7738-8822

The electronic structure and interatomic bonding of pyrophosphate crystal $K_2Mg(H_2P_2O_7)_2{\cdot}2H_2O$ are investigated for the first time showing complex interplay of different types of bindings. The existing structure from single-crystal X-ray diffraction is not sufficiently refined, resulting in unrealistic short O−H bonds which is rectified by high-precision density functional theory (DFT) calculation. $K_2Mg(H_2P_2O_7)_2{\cdot}2H_2O$ has a direct gap of 5.22 eV and a small electron effective mass of 0.14 m_e. Detailed bond analysis between every pair of atoms reveals the complexity of various covalent, ionic, hydrogen bonding and bridging bonding and their sensitive dependence on structural differences. The K–O bonds are much weaker than Mg–O bonds and contributions from the hydrogen bonds are non-negligible. Quantitative analysis of internal cohesion in terms of total bond order density and partial bond order density divulges the relative importance of different types of bonding. The calculated optical absorptions show multiple peaks and a sharp Plasmon peak at 23 eV and a refractive index of 1.44. The elastic and mechanical properties show features unique to this low-symmetry crystal. Phonon calculation gives vibrational frequencies in agreement with reported Raman spectrum. These results provide new insights indicating that acidic pyrophosphates could have a variety of unrealized applications in advanced technology.

1. Introduction

Phosphates is a vast and complex subject with a long history intersecting multiple disciplines of physics, chemistry and biology. However, it is still not fully understood compared to another type of well-known inorganic crystals, the silicates [1]. The first research on phosphates can be traced to two centuries ago with the preparation of $Na_4P_2O_7$ [2]. The vastly different classifications and overlapping nomenclatures of phosphates without consensus across different communities cause great difficulties and confusion among researchers. It is generally agreed that it originated with phosphoric acid H_3PO_4, and the P atom is pentavalently bonded to four O atoms in forming a tetrahedral $[PO_4]^{-3}$ unit. Within this context, condensed phosphates can be described as compounds formed with cations consisting of alkali or other metallic elements and phosphoric anions denoted by $(P_nO_{3n+1})^{-(n+2)}$ $(n < 20)$ or their various combinations with or without the presence of water molecules [1].

Some of the most common and well-known condensed phosphates include aluminium phosphate ($AlPO_4$), potassium titanyl phosphate (KTP, $KTiOPO_4$), calcium pyrophosphate dihydrate ($(Ca_2P_2O_7)\cdot 2H_2O$), hydroxyapatite (HAP, $Ca_{10}(PO_4)_6(OH)_2$), florapatite (FAP, $Ca_{10}(PO_4)_6F_2$) and amorphous calcium phosphates, adenosine triphosphate (ATP), lithium iron phosphates ($LiFePO_7$), potassium dihydrogen phosphate (KDP, KH_2PO_4) and many more. These and other crystalline phosphates have many slightly different designations based on phosphorus content or the O/P ratio such as polyphosphate, pyrophosphate, metaphosphate, diphosphate, triphosphate, oligophosphate, cyclophosphate, etc. [1]. Pyrophosphate, also called diphosphate or dipolyphosphate, is the main subset of this large family of crystals originating from pyro phosphoric acid $P_2O_5\cdot 2H_2O$ ($H_4P_2O_7$) which contains the pentoxide (P_2O_5) group.

Biologists believe that Nature chooses phosphates to be part of the genetic material such as DNA, RNA and ATP because phosphoric acid can meet the stringent condition required for the formation of linkage via hydrolytically stable ester bonds [3]. This leads to the assertion of evolutionary centrality of phosphates [3], as pointed out by Todd that 'Where there is life, there is phosphorus' [4]. Organic phosphates and phosphate-based glasses are also an important part of biomaterials which is another extremely active arena of research [5,6]. There are essentially two types of bio-glasses: (i) a network glass such as ternary phosphate glass $(CaO)_x(Na_2O)_{1-x-y}(P_2O_5)y$ in the form of a continuous random network similar to silicate glasses and (ii) aqueous solution of orthophosphate species $H_n(PO_4)^{3-n}$ $(n = 0–3)$ important for biological reactions. Thus phosphates play an important role in biomedical and life sciences.

Applications of phosphates are ubiquitous because of their diverse compositions and unique complex structures. There are many biomedical and biochemical applications such as special drugs and their deliveries [7], bone repair, tissue engineering [8] and periodontal ligament fibroblasts for cell regeneration [9], etc. In energy science, they are known as predominating materials for Li or Na ion batteries [10,11]. They are also used in a variety of sensors [12,13] and in water oxidation catalysts [14]. Some phosphates such as KTP are known for their exceptionally large second harmonic generation for special electro-optical applications [15,16]. Hence, phosphates are critical to the development of modern technology.

In modern materials research, computational study always accompanies experimentation in any class of materials, and phosphates are no exception. A limited amount of computational works were done in tri- and diphosphates by Hansia *et al*. [17], interaction of pyrophosphate with hydroxyapatite by Rivas *et al*. [18] and cluster model studies on vanadyl pyrophosphates [19]. However, most of the studies in the past concentrate on the structures and geometry with little insights on the fundamental interactions at the atomic level and seldom touch on their properties which are important in their existing and emerging applications. This actually does not come as a surprise, given the confusing status of their definitions and many unsolved issues such as the accuracy of the measured structure, and the appropriate methods for different and diverse structures of phosphate. Most of the computational studies focus on molecular clusters rather than crystalline band structures. They also concentrate more on the vibrational spectra rather than the electronic structure. Quantitative information on different types of bonding in multi-component phosphates are missing. It turns out that we actually have several studies on different types of phosphates within the past decade with the earlier version of the methods we developed. They cover inorganic phosphates [20–22], apatite crystals and their spectroscopic or mechanical properties [23–25], and some major phosphor-olivines Li_xMPO_4 [26,27]. More recently, calculation has been extended to complex biomolecular systems containing phosphorus [28–32].

In this study, we focus on a particular acidic pyrophosphate crystal $K_2Mg(H_2P_2O_7)_2\cdot 2H_2O$ because of its well-characterized crystal structure and detailed vibrational analysis on Raman and infrared

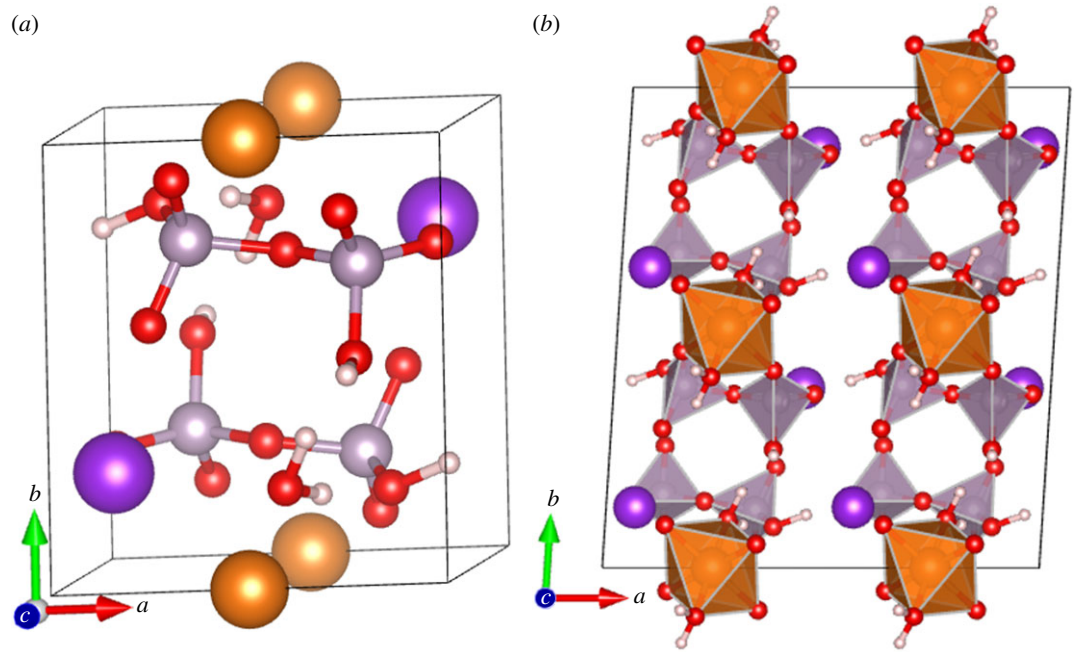

Figure 1. (*a*) Ball and stick diagram for the relaxed cell of $K_2Mg\ (H_2P_2O_7)_2{\cdot}2H_2O$; (*b*) polyhedral diagram for the $2 \times 2 \times 2$ supercell projected along the *c*-axis. MgO_6 octahedra and PO_4 tetrahedra are shown in orange and light purple, respectively. Dark purple sphere for K, small red sphere for O and small pinkish white sphere for H.

spectra first reported by Harcharras *et al*. [33]. To the best of our knowledge, there have not been any electronic structure information for this crystalate or similar pyrophosphates. Here, we report the first such calculation with detailed interatomic bonding together with its optical and mechanical properties. Moreover, we show that, for such crystals, the experimentally determined structure may not be sufficiently accurate due to the difficulty in locating exact positions of H. We first describe its complex structure followed by a brief description of the computational methods used. The calculated electronic structure and properties are presented and discussed in §4. We end with a brief conclusion and discussion on the future prospect of research and potential applications of pyrophosphates in general.

2. Crystal structure of $K_2Mg\ (H_2P_2O_7)_2{\cdot}2H_2O$

The chemical composition of all pyrophosphates contains the ionic group $P_2O_7^{4-}$. Here, we focus on $KMg_{0.5}H_2P_2O_7{\cdot}H_2O$ (or $K_2Mg\ (H_2P_2O_7)_2{\cdot}2H_2O$). This structure belongs to the di-cationic $ABP_y{\cdot}nH_2O$ family where A is a monovalent cation, B can be a mono-, di- or trivalent cation, and P_y is the acidic pyrophosphate group $(H_2P_2O_7)^{2-}$. The crystal has a triclinic structure with space group $P_{-1}(2)$, $Z = 2$ with a total of 31 atoms in the unit cell as shown in figure 1*a*. The original synthesis of this pyrophosphate was done by Harcharras *et al*. [33] in 2003 and the single-crystal structure was obtained using X-ray diffractometry (XRD). The unit cell refinement used 1055 of the 1446 reflections observed by omitting those with intensity I less than $2\sigma/(I_{obs})$. The final structure was resolved using the direct method of SIR97 [34] and refined by a full-matrix least square technique based on F2-SHELXL-97 [35] with residue $R = 0.0368$ and supposed to be extremely accurate. Four years later, one of us (R.K.) used a new synthesis method, the co-precipitation method according to the reaction scheme: $2\,K_4P_2O_7 + MgCl_2 + 4HCl$ to give $K_2Mg\ (H_2P_2O_7)_2{\cdot}2H_2O + 6KCl$ (dissolved). The recovered single crystal was then analysed in the same laboratory using the same high-precision procedure. The structure differs only slightly from the one published earlier by Harcharras *et al*. [33] (see electronic supplementary material for comparison). This structure is now referred to as the experiment XRD or unrelaxed structure in the present discussion. Figure 1*b* shows the polyhedral picture of this crystal in a $2 \times 2 \times 2$ supercell showing layers of MgO_6 octahedra and PO_4 tetrahedra, and the locations of the K ions.

However, it was observed that there are two very short O−H bonds of 0.636 Å, 0.650 Å in the experimentally measured data which appear to be unrealistic. We proceed to investigate this problem using density functional theory (DFT) by firstly optimizing the measured structure theoretically using

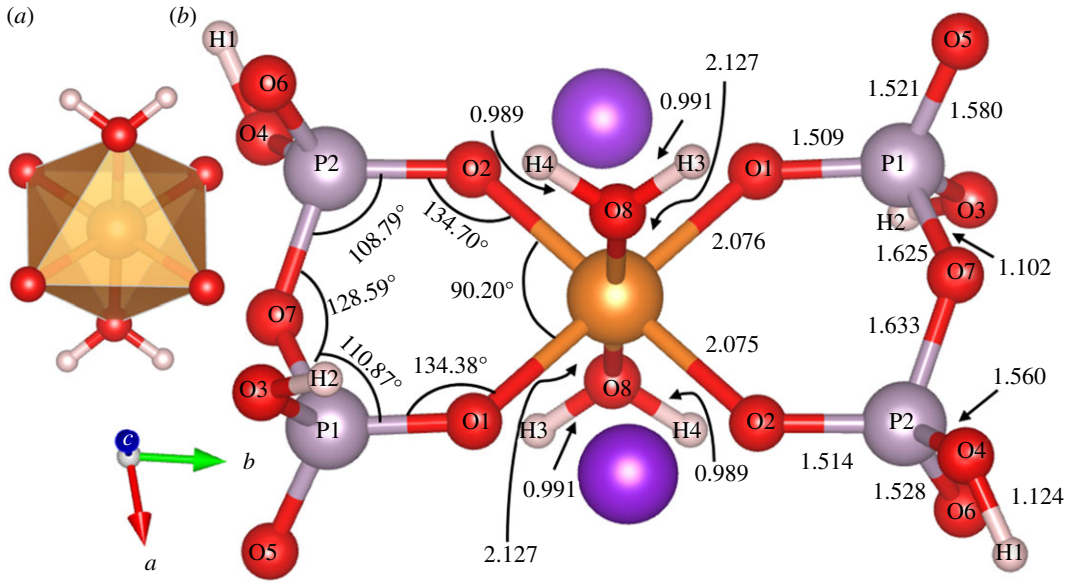

Figure 2. (*a*) Sketch of Mg-centred octahedron. (*b*) Two-dimensional sketch of Mg-centred $K_2Mg(H_2P_2O_7)_2{\cdot}2H_2O$ in the plane of diphosphate. The bond lengths shown are in units of Å. Large orange (dark purple) sphere for Mg (K), light purple sphere for P, small red sphere for O and small pinkish white sphere for H.

VASP (Vienna *ab initio* simulation package) [36]. We used PAW (projector augmented wave) with PBE potential [37] for the exchange and correlation functional within the generalized gradient approximation of the DFT. To achieve high accuracy for the structure optimization, a high cut-off energy of 600 eV is used. The electronic convergence and ionic force convergence are set at of 10^{-9} eV and 10^{-7} eV Å^{-1}, respectively. A $3 \times 3 \times 3$ *k*-point sampling using the standard Monkhorst scheme [38] as implemented in VASP is adopted. Test calculations by using other exchange correlation functionals such as hybrid functionals PBE0, HSE03 and also applying van der Waals correction show only very minor change in the relaxed structure.

In table 1, we compare the experimental structure (XRD) and the final optimized structure (DFT) for $K_2Mg(H_2P_2O_7)_2{\cdot}2H_2O$. It can be seen that there are some notable changes in the lattice constants with a slight increase in cell volume by 3.35%. Most importantly, the two unrealistically short O−H bonds of 0.636 Å and 0.656 Å are increased to a reasonable value of 1.102 Å and 1.124 Å, respectively. Simultaneously, the two hydrogen bonds (HBs), O···H, with bond lengths (BLs) 1.781 Å and 1.821 Å decreased to 1.304 Å and 1.349 Å of bridging bonds (i.e. O−H bonds from O−H−O, shown in figure 7 in blue circles), respectively. Another pair of HBs with BLs of 1.897 Å and 1.906 Å are also decreased to 1.807 Å and 1.768 Å, respectively. These changes have significant consequence in the subsequent analysis of interatomic bonding in this crystal (see §4.4). The total energy of the relaxed crystal is 19.12 eV lower than in the unrelaxed structure, or 59.51 KJ mol^{-1} per atom, indicating that the relaxed structure is more stable than the unrelaxed one. All different bond lengths for all atomic pairs are listed in table 1 for direct one-to-one comparison with those O−H, O···H and O−H−O bridging bonds with significant changes mentioned above shown in bold. Figure 2 shows a two-dimensional sketch of the relaxed structure with different bond angles and bond lengths clearly marked. In the MgO_6 octahedron, Mg forms ionic bonds with four O atoms from the four PO_4 tetrahedra and two O atoms from the two water molecules. In the two PO_4 tetrahedra within the $(H_2P_2O_7)^{2-}$ group, one of its O atoms (O7) is bonded with another P atom in forming the strong P−O−P bond, which has been the centre of discussion in many pyrophosphate crystals and molecules. The two six-member rings with bonds P2−O7−P1−O1−Mg−O2−P2 and P1−O7−P2−O2−Mg−O1−P1 in figure 2 are symmetric with same bond lengths and bond angles. Ostensibly, some of the K−O separations are quite large (greater than 3.0 Å) and the formation of a K-centred polyhedron of these crystals is unlikely.

3. Method of electronic structure and properties calculation

For the electronic structure, interatomic bonding and optical properties of the titled crystal, we use the Orthogonalized linear combination of atomic orbital (OLCAO) method [39], which is also a DFT-based

Table 1. Comparison between experimental XRD- and DFT-relaxed structures.

	XRD	DFT
a, b, c	6.890 Å, 7.363 Å, 7.704 Å	6.954 Å, 7.503 Å, 7.589 Å
α, β, γ	80.900°, 71.660°, 84.270°	81.166°, 75.522°, 84.257°
V(Å^3)	365.788	378.045
Bonds	BL(Å)	BL(Å)
O—H	**0.636**, **0.650**, **0.961**, **1.044**	**1.102**, **1.124**, **0.991**, **0.989**
P—O	1.499, 1.503, 1.506, 1.509, 1.547, 1.548, 1.601, 1.613, 3.405, 3.489	1.560, 1.509, 1.580, 1.514, 1.521, 1.528, 1.633, 1.625, 3.475, 3.469,
O· · · H	**1.781**, **1.821**, **1.897**, **1.906**, 2.927, 3.034, 3.095, 3.250, 3.391, 3.439	**1.807**, **1.768**, 3.062, 3.187, 3.289, 3.333, 3.372, 3.402,
O—H—O	–	**1.304**, **1.349**
Mg—O	2.053, 2.054, 2.091	2.076, 2.075, 2.127
K—O	2.808, 2.849, 2.944, 3.039, 3.060, 3.210, 3.352, 3.423	2.767, 2.830, 3.041, 2.941, 2.911, 3.482, 2.790
energy (eV)	−170.1357	−189.2564

method. The VASP-optimized structure described above is used as input for the OLCAO calculation. The OLCAO method uses atomic orbitals for the basis expansion and is very efficient as well as economical, especially for large complex systems. It has been used previously to study the electronic structure and spectroscopic properties of many phosphate-related inorganic crystals and their surfaces [21–27]. The use of the OLCAO method with a VASP-optimized structure has resulted in many successful calculations in electronic and optical properties for large complex materials including inorganic glasses [40–44] and biomolecules [30–32].

In most OLCAO calculations, a more localized minimal basis (MB) is used for the calculation of effective charges Q^*_α and the bond-order (BO) values $\rho_{\alpha\beta}$ between a pair of atoms (α, β) using Mulliken population analysis [45,46].

$$Q^*_\alpha = \sum_i \sum_{m,\mathrm{OCC}} \sum_{j,\beta} C^{*m}_{i\alpha} C^m_{j\beta} S_{i\alpha,j\beta} \tag{3.1}$$

and

$$\rho_{\alpha\beta} = \sum_{m,\mathrm{OCC}} \sum_{i,j} C^{*m}_{i\alpha} C^m_{j\beta} S_{i\alpha,j\beta}. \tag{3.2}$$

In equations (3.1) and (3.2), $S_{i\alpha,j\beta}$ are the overlap integrals between the ith orbital in the αth atom and the jth orbital in the βth atom; and $C^{\mathrm{m}}{}_{j\beta}$ are the eigenvector coefficients of the mth band, jth orbital in the βth atom. We have calculated the partial charge ΔQ or the charge transfer which is a deviation from neutral charge (Q^{o}) of the effective charge (Q^*) on the same atom i.e. $\Delta Q = Q^{\mathrm{o}} - Q^*$. The MB set used in the present study has the atomic configurations of P: $1s^2\ 2s^2\ 2p^6\ 3s^2\ 3p^3$; Mg: $1s^2\ 2s^2\ 2p^6\ 3s^2$; K: $1s^2\ 2s^2\ 2p^6\ 3s^2\ 3p^6\ 3d\ 4s^1$; O: $1s^2\ 2s^2\ 2p^4$ and H: $1s^1$. A full-basis (FB) set which has one more shell of atomic orbitals than the MB is used for calculation of self-consistent potential, the total density of states (TDOS), partial density of states (PDOS), band structure and optical properties.

The bond order (BO) $\rho_{\alpha\beta}$ in equation (3.2) provides a quantitative measure for the strength of the bond. The summation of all BOs normalized by the cell volume gives us the total bond order density (TBOD), which is a single metric to assess the internal cohesion in the crystal [47]. TBOD can be resolved into partial components, or the partial BO density (PBOD) from different types of atomic pairs or groups of atoms in a structural unit.

For the interband optical properties in the form of frequency-dependent complex dielectric function $(\hbar\omega) = \varepsilon_1(\hbar\omega) + \mathrm{i}\varepsilon_2(\hbar\omega)$, the imaginary part $\varepsilon_2(\hbar\omega)$ is calculated first according to

$$\varepsilon_2(\hbar\omega) = \frac{e^2}{\pi n \omega^2} \int_{BZ} \mathrm{d}k^3 \sum_{nl} |\langle \psi_n(k,r)| - i\hbar\nabla|\psi_1(k,r)\rangle|^2 f_l(k)[1 - f_n(k)]\delta[E_n(k) - E_l(k) - \hbar\omega], \tag{3.3}$$

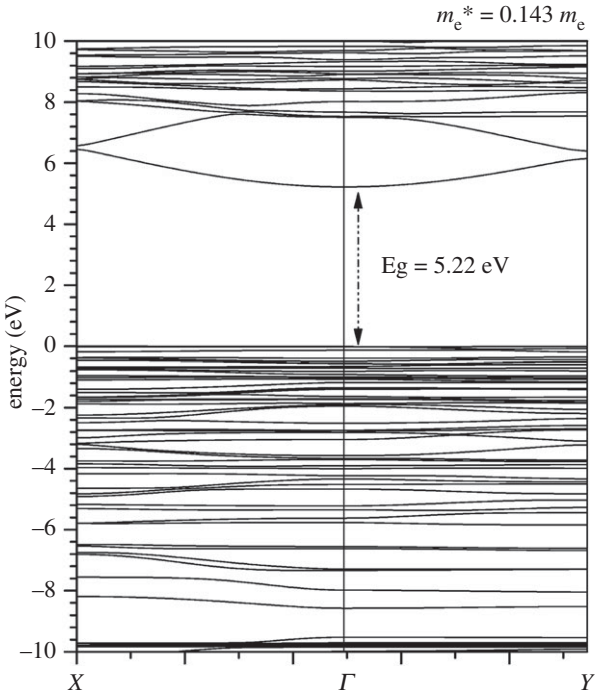

Figure 3. Calculated band structure for $K_2Mg\ (H_2P_2O_7)_2{\cdot}2H_2O$. The electron effective mass at Γ is $m_e^* = 0.143m_e$.

where l and n are for the occupied and unoccupied states, respectively, $\psi_n(k, r)$ are the *ab initio* Bloch functions from OLCAO calculation using FB and a large k-point sampling, and $f_1(k)$ and $f_n(k)$ are the Fermi distribution functions. The real part $\varepsilon_1(\hbar\omega)$ is obtained from the imaginary part $\varepsilon_2(\hbar\omega)$ through Kramers–Kronig transformation [48]. The energy loss function, $F(\omega)$ is obtained from the imaginary part of $(1/\varepsilon)$.

$$F(\omega) = \mathrm{IM}\left(-\frac{1}{\varepsilon(\omega)}\right) = \frac{\varepsilon_2(\omega)}{\varepsilon_1^2(\omega) + \varepsilon_2^2(\omega)}. \tag{3.4}$$

The elastic and mechanical properties of the pyrophosphate crystal are calculated using the stress versus strain approach to obtain the complete set of elastic coefficient C_{ij} and compliance tensor. The fully relaxed crystal structure from VASP is used to calculate the second-order elastic tensors for the crystal using an efficient scheme [49,50] by applying a strain of ±0.5% to the cell to obtain the stress data σ_j. The elastic coefficients C_{ij} are obtained by solving the set of linear equation

$$\sigma_i = \sum_{j=1}^{6} C_{ij}\varepsilon_j \quad (i, j = 1, 2, 3, 4, 5, 6). \tag{3.5}$$

The usual mechanical properties K (bulk modulus), G (shear modulus), E (Young's modulus) and η (Poisson's ratio) are obtained based upon the Voigt–Reuss–Hill approximation for polycrystals [51,52].This approach for mechanical properties has been successfully used by us in many different inorganic crystals and glasses [44,53–57].

4. Results and discussion

4.1. Band structure and density of states

The calculated band structure for the triclinic $K_2Mg\ (H_2P_2O_7)_2{\cdot}2H_2O$ crystal is shown in figure 3. It has a direct band gap (Eg) at Γ of 5.22 eV, larger than the other phosphate crystal HCP (4.51 eV) and smaller than FAP (5.47 eV) [23] calculated using the same method. The wide band gap shows the insulating nature of $K_2Mg\ (H_2P_2O_7)_2{\cdot}2H_2O$. The top of the valence band (VB) is quite flat, whereas the bottom of the conduction band (CB) has a curved feature with an effective electron mass of $m_e^* = 0.143\ m_e$, comparable to the wide-gap semiconductors such as in AlP ($0.13m_e$), GaN ($0.19m_e$), ZnO ($0.24m_e$), ZnSe ($0.17m_e$) and ZnTe ($0.18m_e$). This could imply that it will have large electron mobility in the CB with useful applications.

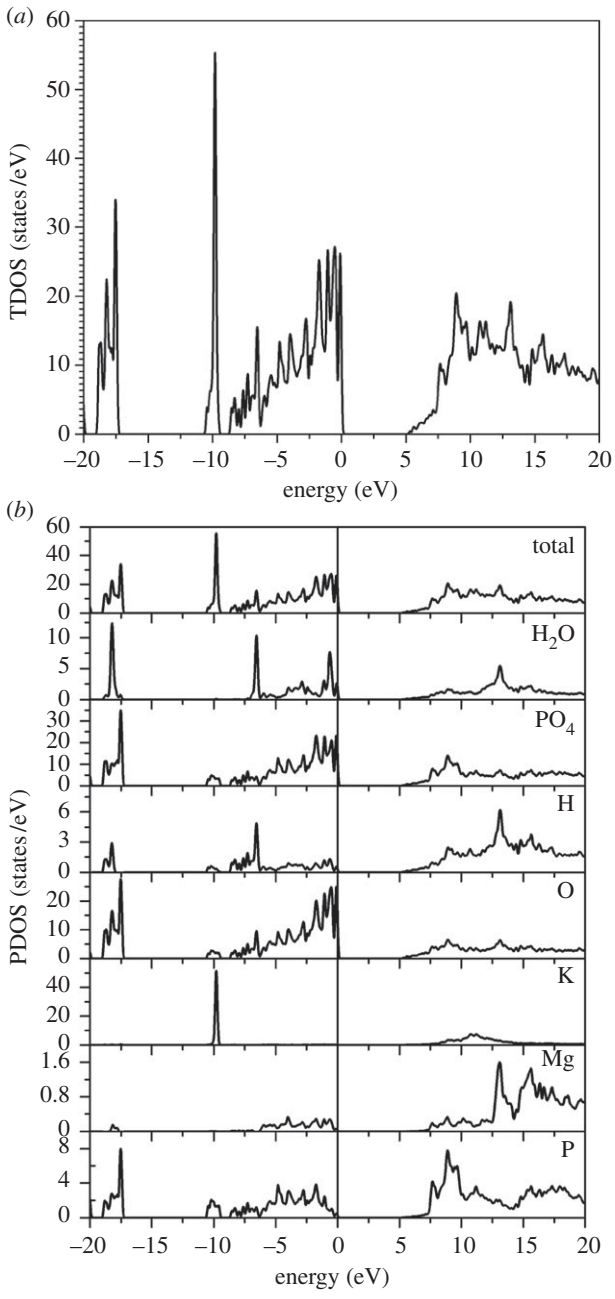

Figure 4. Calculated (*a*) total density of states (TDOS) and (*b*) partial density of states (PDOS) for H_2O and PO_4 groups and for each type of atom in $K_2Mg(H_2P_2O_7)_2{\cdot}2H_2O$.

The calculated TDOS in the energy range of −20 to 20 eV is shown in figure 4*a*. Details of TDOS are best discussed in terms of the PDOS for each type of atoms and the two groups (H_2O) and (PO_4) shown in figure 4*b*. The peaks in the region lower than –15 eV come from P, O and H atoms, indicating the strong P−O bonding in the PO_4 tetrahedron and O−H bonding in H_2O. There is a very sharp peak at −10 eV from K-3p which simply reflects the semi-core nature of the K-3p orbital. All elements are responsible for the peaks in the energy range −10 to 0 eV, or the upper VB. The top of the VB is dominated by the states from PO_4 tetrahedrons in the pyrophosphate group $(H_2P_2O_7)^{-2}$. Inspection of the wave function for the HOMO and LUMO states reveals that they come from the binding and anti-binding orbitals of the O−P bonds, which is a universal feature in almost all phosphates.

4.2. Partial charge

The partial charges (PCs) obtained from the effective charges according to equation (3.1) for the 31 atoms in the $K_2Mg(H_2P_2O_7)_2{\cdot}2H_2O$ crystal are listed in table 2 and plotted in figure 5. All atoms except O

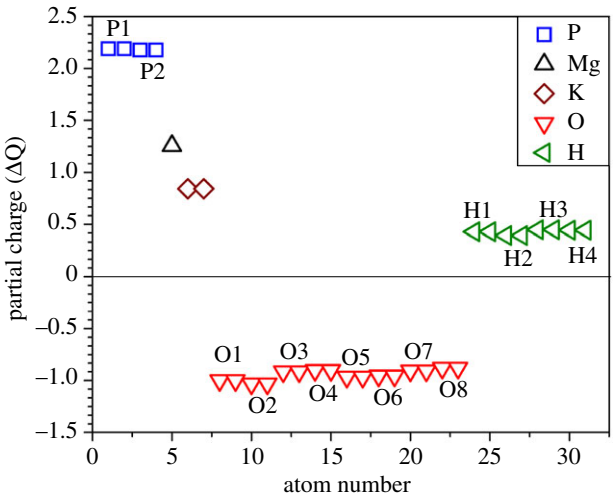

Figure 5. Calculated partial charge (ΔQ) distribution in $K_2Mg(H_2P_2O_7)_2{\cdot}2H_2O$. The numbered atoms are in accordance with table 2.

Table 2. Different partial charge of each element in the DFT-relaxed structure.

element	ΔQ	element	ΔQ
P1	2.189	01	−0.999
P2	2.179	02	−1.031
Mg	1.256	03	−0.914
K	0.842	04	−0.902
H1	0.429	05	−0.966
H2	0.393	06	−0.955
H3	0.449	07	−0.906
H4	0.444	08	−0.880

have positive PCs that donate electrons to O. The largest positive PC is from P (+2.179 e and +2.189 e) in forming PO_4 tetrahedra, which have negative charge as a unit. The divalent Mg ion has a larger PC (+1.256 e) than the monovalent K potassium (+0.842 e), and the PC for H atoms differ slightly (+0.393 e to +0.449 e) depending on the atoms they bond to. Note that the PC for the eight types of O are all different because they are crystallographically non-equivalent. This can be best seen in figure 2 where the positions of the labelled atoms in the sequential order are marked. Figure 5 shows that there are two data points each for O1 to O8. The O1 atoms form the P1−O1−Mg bonds connecting the PO_4 tetrahedron to the MgO_6 octahedron in the 6-member ring. Similarly, O2 form the other P2−O2−Mg bonds in the same 6-member ring. O3 and O4 form a P1−O3−H2 bond and P2−O4−H1 bond, respectively, involving the two elongated O−H bonds with BLs of 1.102 Å and 1.124 Å that has been emphasized in §2 above in the structure change due to optimization. O6 is the atom bonded only to P2, whereas O7 is forming the bridging bond between two phosphorus atoms P1 and P2. Finally, O8 is the atom in the two water molecules but they also participate in the formation of the octahedra centred at Mg. The above discussion on the PC distribution of all atoms within the unit cell of triclinic $K_2Mg(H_2P_2O_7)_2{\cdot}2H_2O$ crystal provided the most detailed and quantitative analysis of the charge transfer in the crystal in relation to their geometric arrangements.

4.3. Interatomic bonding

The BO values are a measure of strength and stiffness of the bond for each atomic pair. The calculated BO distribution versus bond length (BL) for different pairs of bonds in $K_2Mg(H_2P_2O_7)_2{\cdot}2H_2O$ are displayed in figure 6, figure 6*a* for the results from the original experimental structure and figure 6*b*

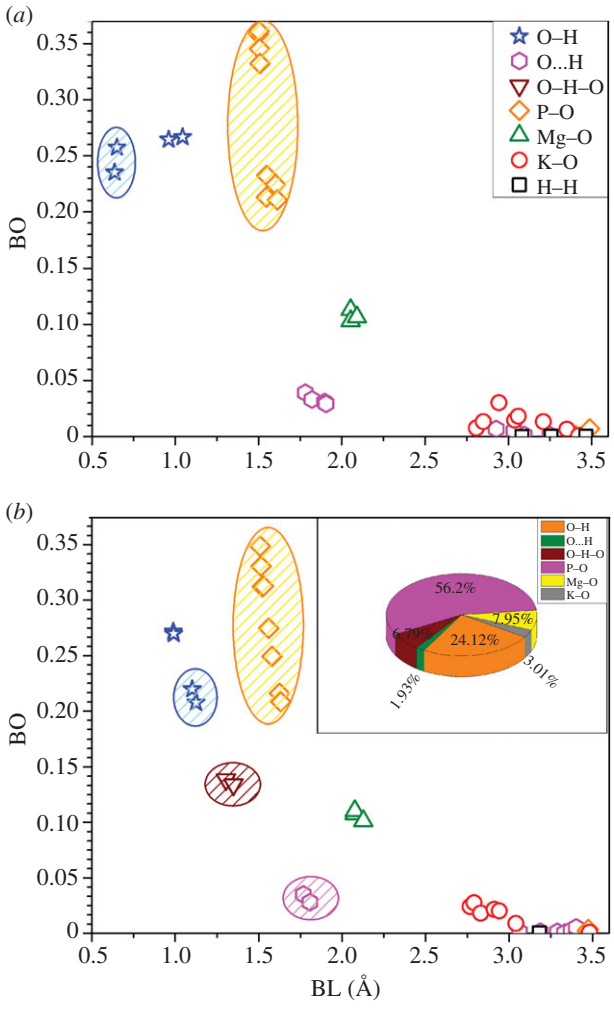

Figure 6. Calculated bond order (BO) versus bond length (BL) of $K_2Mg(H_2P_2O_7)_2{\cdot}2H_2O$ for (*a*) unrelaxed and (*b*) relaxed crystal. Each bond type is denoted by different symbols. Elliptical enclosures denote different groups of bond pairs (see text for details.) Inset: % contribution to the TBOD from different covalent, ionic and hydrogen bonds.

for the optimized or the final relaxed structure. There are seven different types of bonding with varying strengths: two covalent bonds (O−H, P−O), two ionic bonds (Mg−O, K−O), the ubiquitous HB (O···H), bridging bonds O−H−O (in optimized structure only) and negligibly weak H−H bonds. The two unusually short O−H bonds of BLs 0.63 Å and 0.64 Å with high BO values depicted in figure 6*a* have been corrected after optimization to 1.10 Å and 1.12 Å (O3−H2 and O4−H1 in figure 2) and reasonable BO values (figure 6*b*, blue ellipse). Another major change due to optimization is that, in the unrelaxed experimental structure, the four HBs (O···H) are relatively weak with typical HB length of 1.8 Å. After optimization, two of the HBs become much stronger with BO values of 0.139 and 0.134, and BLs of 1.304 Å and 1.349 Å, respectively, forming a bridging bond O−H−O (brown inverse triangle in figure 6*b*). The other two HBs remain similar (pink ellipse in figure 6*b*). These HB configurations are more clearly shown in figure 7 on the extended cell geometry. The change in the covalent P−O bonds between unrelaxed and optimized structures are much smaller, accentuating the rigidity of the PO_4 tetrahedron as a strong structural unit in phosphate crystals. The minor changes in the spread of BO values can be attributed to structural changes of the more prominent changes in O−H bonds, HBs and bridging bonds. As for the ionic bonds, the changes due to optimization is minimal. Mg−O bonds are relatively stronger than the K−O bonds and they do form the octahedral unit. K−O bonds are very weak and they cannot be considered to form any type of polyhedrons in phosphates at least in the present diphosphate crystal but may do so in some non-crystalline phosphate bio-glasses [33].

TBOD is the sum of total bond order in the system normalized by volume. We use the TBOD to assess the cohesion in the system. Table 3 compares the TBO and TBOD and their components, the PBOD for

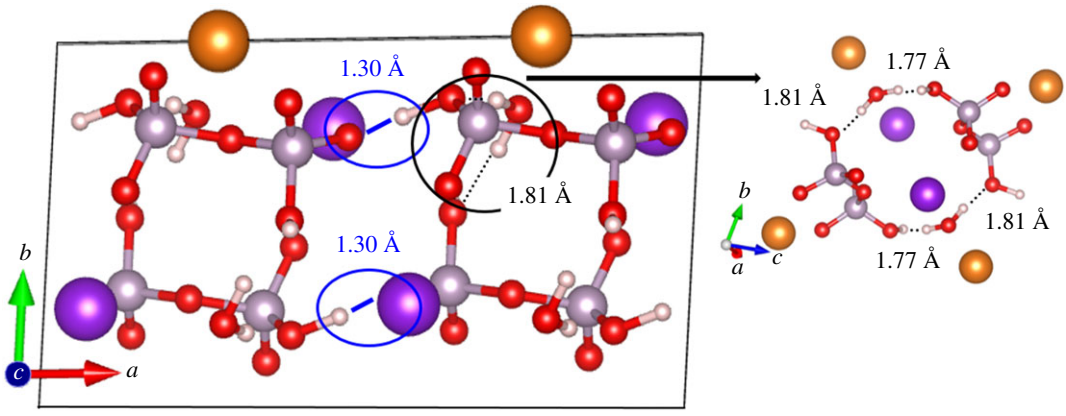

Figure 7. Illustration of the short and stronger bridging O—H—O bond of 1.30 Å (shown in blue) after optimization between two $H_2P_2O_7$ groups in the adjacent cells (the lower bridging bond is not clear; there is an oxygen atom behind a potassium atom). Dark purple sphere for K, small red sphere for O and small pinkish white sphere for H. The figure on the right shows O···H bonds of 1.77 Å and 1.81 Å.

Table 3. Comparison between TBOD and PBOD using experimental and DFT-relaxed structures.

bonds	PBOD (XRD) (electron/(Å)^3)	PBOD (DFT) (electron/(Å)^3)
O—H	0.00560	0.00512
O···H	0.00081	0.00041
O—H—O	–	0.00144
P—O	0.01250	0.01194
Mg—O	0.00176	0.00169
K—O	0.00057	0.00064
TBOD	0.02124	0.02125
TBO (e^-)	7.76920	8.03360

the unrelaxed and the optimized structure. As can be seen, the TBO in the optimized structure is higher than that in the original structure by 3.4%, consistent with the total energy shown in table 1. The inset of figure 6*b* shows the percentage contribution from a covalent bond, ionic bond and HB in terms of the PBOD. The P—O bonding has a major contribution of 56.2% in the system and provides the main cohesion in the crystal. Thus the P—O bonds are the most important bonding in the formation of the pyrophosphate. This is the main reason that pyrophosphates are the key structural unit in almost all inorganic phosphates and in forming the backbone in biological or genetic materials. On the other hand, O—H bonds (24.12%) also have significant cohesion for the system. Bridging O—H—O bonds (6.79%) and Mg—O (7.95%) bonds have a similar contribution. However, O···H (1.93%), K—O (3.01%) bonds have an insignificant contribution to the cohesion in this system. The comparison with a similar calculation of BO values with the other experimental structure from Harcharras *et al*. [33] is shown in electronic supplementary material, table S1. It is quite obvious that the optimized structure has the largest TBO and TBOD indicating a stronger crystal cohesion.

4.4. Optical properties and refractive index

The optical properties of $K_2Mg(H_2P_2O_7)_2{\cdot}2H_2O$ are calculated in the form of complex dielectric function based on interband optical transitions. Figure 8*a* shows the calculated real (ε_1) and imaginary (ε_2) parts of frequency-dependent dielectric function in black and red lines. The optical absorption spectrum (ε_2) shows five well-defined peaks A, B, C, D, E roughly at 7, 10, 13, 16, 21 eV, with peaks A and E the most prominent. These absorptions occur in the vacuum ultraviolet and part of the extreme ultraviolet region, well beyond the visible range and consistent with the transparent nature of the crystal. From the

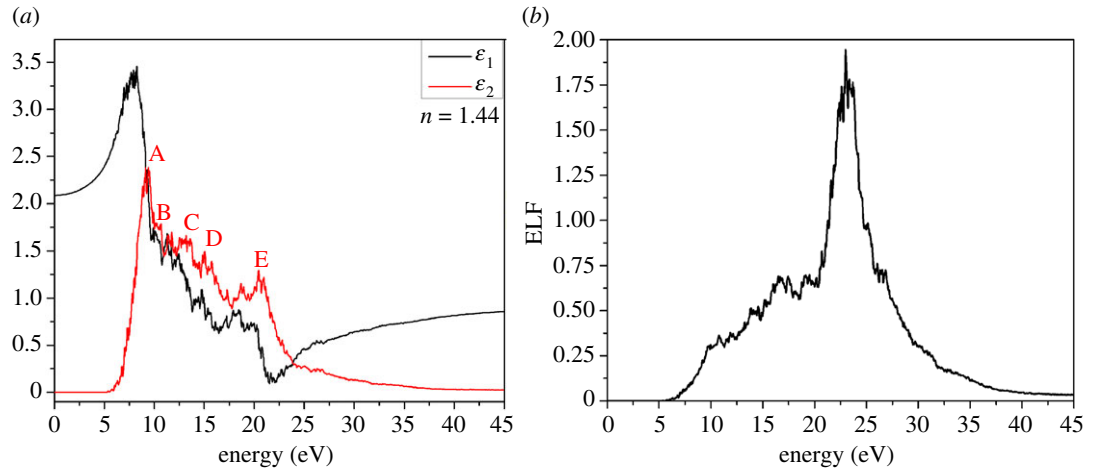

Figure 8. (*a*) Calculated real (ε_1) (black curve) and imaginary (ε_2) (red curve) parts of the complex dielectric function and (*b*) energy loss function (ELF) for $K_2Mg(H_2P_2O_7)_2{\cdot}2H_2O$.

calculated dielectric functions, we can obtain the static dielectric constant by taking the zero-frequency limit of the real part of the dielectric function. The refractive index is estimated by taking the square root of $\varepsilon_1(0)$. For $K_2Mg(H_2P_2O_7)_2{\cdot}2H_2O$, the calculated refractive index is 1.44. This can be compared with refractive indices of some common materials such as 1.33 for water, 1.458 for fused silica, 1.44–1.47 for olive oil and 1.42 for the 50% sugar solution. Hence, it is conceivable that dicationic pyrophosphates and other related crystalline or amorphous phosphates can find potential applications in technology similar to those of the silicate glasses or in biological fluids.

Figure 8*b* shows the energy loss function (ELF) obtained from the complex dielectric function. The main peak in ELF is identified as the plasma frequency (ω_p) and is 22.98 eV. This is the frequency for the collective excitation of the electrons in a solid and is experimentally an easily measurable quantity. Thus, calculation of optical properties of different pyrophosphates can be effectively used as a predictor for the possible phases in an unknown sample.

4.5. Mechanical properties

As pyrophosphates may have many diversified uses, it is essential to know their mechanical properties like bulk modulus (K), shear modulus (G), Young's modulus (E) and Poisson's ratio (η). Table 4 lists the calculated elastic tensor C_{ij} from equation (3.5). $K_2Mg(H_2P_2O_7)_2{\cdot}2H_2O$ has a triclinic structure of very low symmetry, so all the 22 second-order tensor elements are non-zero. The largest one is C_{11} followed by C_{22} and C_{33}, which are very close. It was noted that the off-diagonal element C_{13} is actually negative but small, which could be related to the rather complex structure of $K_2Mg(H_2P_2O_7)_2{\cdot}2H_2O$, with the presence of water molecules discussed in §2. The calculated K and G are 22.88 GPa and 15.63 GPa, respectively. The low K and G show $K_2Mg(H_2P_2O_7)_2{\cdot}2H_2O$ with a G/K ratio of 0.691, which shows the materials to be brittle and not soft. This seems to be counterintuitive to the fact that $K_2Mg(H_2P_2O_7)_2{\cdot}2H_2O$ contains water molecules and a larger number of weak ionic bonds. The calculated E is 38.19 GPa and the Poisson's ratio η is 0.2218. This value is smaller than similar calculations on HAP (0.262) [58] which contains the unlinked PO_4 tetrahedrons. The low Poisson's ratio η and high E for $K_2Mg(H_2P_2O_7)_2{\cdot}2H_2O$ also suggest that the material is less ductile and stiff in nature. This could be linked to the rigidity of the pyrophosphate units in contrast to the isolated PO_4 unit. This is the first time that the mechanical properties of a pyrophosphate crystal have been calculated and much deeper analysis of their intriguing behaviour needs further investigation. We are not aware of any experimental measurements on the mechanical properties of pyrophosphate crystals.

4.6. Connection to experimental vibrational spectrum

It is not clear at this moment if the above new findings may influence the interpretation of the vibrational properties because Raman and infrared measurements were conducted on actual samples and did not explicitly depend on the reported crystal parameters [33]. It would be of great interest to establish a

Table 4. Calculated elastic coefficients of $K_2Mg(H_2P_2O_7)_2{\cdot}2H_2O$ in units of GPa.

$$\begin{pmatrix} C_{11} & C_{12} & C_{13} & C_{14} & C_{15} & C_{16} \\ C_{21} & C_{22} & C_{23} & C_{24} & C_{25} & C_{26} \\ C_{31} & C_{32} & C_{33} & C_{34} & C_{35} & C_{36} \\ C_{41} & C_{42} & C_{43} & C_{44} & C_{45} & C_{46} \\ C_{51} & C_{52} & C_{53} & C_{54} & C_{55} & C_{56} \\ C_{61} & C_{62} & C_{63} & C_{64} & C_{65} & C_{66} \end{pmatrix} = \begin{pmatrix} 84.07 & 6.58 & -2.50 & 2.55 & 8.92 & 6.81 \\ 6.58 & 58.55 & 16.80 & 6.16 & 1.81 & 5.29 \\ -2.50 & 16.80 & 58.14 & 5.50 & 10.92 & 1.35 \\ 2.55 & 6.16 & 5.50 & 16.25 & 0.34 & 2.25 \\ 8.92 & 1.81 & 10.92 & 0.34 & 9.77 & 2.66 \\ 6.81 & 5.29 & 1.35 & 2.25 & 2.66 & 11.07 \end{pmatrix}$$

connection between the electronic structure and bonding to the discussion of the vibrational spectra, which have many interesting features at the low-frequency region. To this end, we have calculated the phonon spectrum of the $K_2Mg(H_2P_2O_7)_2{\cdot}2H_2O$ crystal using the phonopy package [59], with VASP for the force calculation. This requires even higher accuracy because it involves a higher vibration frequency of O−H modes and the HBs. The convergence criteria for electronic and ionic force are now set at 10^{-9} eV and 10^{-7}eV Å^{-1}, respectively. The calculated phonon spectrum and phonon DOS are shown in electronic supplementary material, figure S1a,b, respectively. The vibrational frequencies at the zone centre Γ gives the information on Raman and infrared active modes. The vibrational frequency range can be divided into three regions I (0–37.72 THz), II (38.34–57 THz) and III (97.67–105.79 THz) (electronic supplementary material, figure S1b). This is in very good agreement with the measured Raman spectrum as shown in fig. 5 of Harcharras *et al.* [33], both showing multiple peak structures in region I, very pronounced double peak structure in region II and H-related vibration modes in region III separated from region II with a large gap.

5. Conclusion

In this article, we have presented a detailed analysis of the electronic structure, interatomic bonding, optical and mechanical properties calculation for the acidic diphosphate $K_2Mg(H_2P_2O_7)_2{\cdot}2H_2O$. This is the first such study in this pyrophosphate crystal of very low symmetry. It is concluded that the existing crystal structure data from XRD is not sufficiently refined, which results in unrealistically short O−H bonds. This is rectified by high-precision computational optimization. The results show the insulating nature of this crystal with a large HOMO−LUMO gap of 5.22 eV. The P−O bond has a large bond order and the highest percentage contribution to the TBOD among all other bonds, indicating the high rigidity of the $(P_2O_7)^{4-}$ ion in the pyrophosphate. The important role of strong O−H covalent bonds, substantial O−H−O bridging bonds and O$\cdots$H HBs in this pyrophosphate is pointed out. It also shows that the formation of a K-centred polyhedron is unlikely due to the very weak K−O bonds. On the other hand, the Mg−O bonds are reasonably strong in forming the octahedral unit of MgO_6 with two O atoms from the water molecules.

The most significant part of the above finding is that conventional XRD data and its structural analysis may be questionable for crystals involving light H atoms because of their weak intensity signals in the measurement. This could affect many of the published data on the structures of pyrophosphates. High-level DFT calculation can ameliorate the situation and should be part of future crystallographic analysis. The combination of an optical spectrum with large absorption at much higher energy beyond the ultraviolet region and the interesting mechanical properties unique to this low-symmetry crystal, and their possible connection to the low-frequency vibrational spectra offer new insights and opportunities for novel applications of the pyrophosphate materials.

We end this section with comments on possible extension of the present work and what specific aspects of the properties calculation can be related to real applications. Firstly, there are many similar diphosphate crystals such as $K_2Cu(H_2P_2O_7)_2{\cdot}2H_2O$ [60], $(NH_4)_2Zn(H_2P_2O_7)_2{\cdot}2H_2O$ [61], $(NH_4)_2Mn(H_2P_2O_7)_2{\cdot}2H_2O$ [62] and $K_2Zn(H_2P_2O_7)_2{\cdot}2H_2O$ [63], where the presence of transition metals could significantly affect its electronic structure and properties, leading to some unexpected applications. Secondly, the calculation can be extended to triphosphates or even to non-crystalline pyrophosphate glasses where the application in biological or medical areas are abundant. The OLCAO method is fully capable of treating such complex systems as demonstrated in many recent applications to large biomolecular systems [28,29,31,32] and inorganic glasses [41–43,56].

Ethics. This is a computational theoretical study and is not required to complete an ethical assessment.

Data accessibility. The datasets supporting this article have been uploaded as part of the electronic supplementary material.

Authors' contributions. R.K., H.E-.Z. and W.-Y.C. conceived and initiated the project. P.A. and W.-Y.C. did the calculations. R.K. and H.E-.Z. provided the crystal structure. P.A. and W.-Y.C. drafted the manuscript. P.A. made all the graphics. All the authors participated in the discussion, reviewed the manuscript and approved the final version for publication.

Competing interests. We have no competing interests.

Funding. P.A. is supported by a research grant from the School of Graduate Studies at UMKC. This research used the resources of the National Energy Research Scientific Computing Center supported by DOE under Contract No. DE-AC03-76SF00098 and by Research Computing Support Services (RCSS) of the University of Missouri System.

References

1. Durif A. 1995 *Crystal chemistry of condensed phosphates*. Berlin, Germany: Springer Science & Business Media.
2. Berzelius J. 1816 Untersuchungen über die Zusammensetzung der Phosphorsäure, der phosphorigen Säure und ihrer Salze. *Annalen der Physik*. **53**, 393–446. (doi:10.1002/andp.18160540904)
3. Westheimer FH. 1987 Why nature chose phosphates. *Science* **235**, 1173–1178. (doi:10.1126/science.2434996)
4. Todd AR. 1981 Where there's life, there's phosphorus. In *Science and scientist: essays by biochemists, biologists and chemists* (eds M Kageyama, K Nakamura, T Oshima), pp. 275–279. Tokyo, Japan: Japan Science Society Press.
5. Allan I, Newman H, Wilson M. 2001 Antibacterial activity of particulate Bioglass® against supra- and subgingival bacteria. *Biomaterials* **22**, 1683–1687. (doi:10.1016/S0142-9612(00)00330-6)
6. Hench LL, Polak JM. 2002 Third-generation biomedical materials. *Science* **295**, 1014–1017. (doi:10.1126/science.1067404)
7. Illum L, Farraj NF, Davis SS. 1994 Chitosan as a novel nasal delivery system for peptide drugs. *Pharma. Res.* **11**, 1186–1189. (doi:10.1023/a:1018901302450)
8. Kim B-S, Mooney DJ. 1998 Development of biocompatible synthetic extracellular matrices for tissue engineering. *Trends Biotechnol.* **16**, 224–230. (doi:10.1016/S0167-7799(98)01191-3)
9. Murakami Y, Kojima T, Nagasawa T, Kobayashi H, Ishikawa I. 2003 Novel isolation of alkaline phosphatase-positive subpopulation from periodontal ligament fibroblasts. *J. Periodontol.* **74**, 780–786. (doi:10.1902/jop.2003.74.6.780)
10. Hautier G, Jain A, Ong SP, Kang B, Moore C, Doe R, Ceder G. 2011 Phosphates as lithium-ion battery cathodes: an evaluation based on high-throughput *ab initio* calculations. *Chem. Mater.* **23**, 3495–3508. (doi:10.1021/cm200949v)
11. Fang Y, Zhang J, Xiao L, Ai X, Cao Y, Yang H. 2017 Phosphate framework electrode materials for sodium ion batteries. *Adv. Sci.* **4**, 1600392. (doi:10.1002/advs.201600392)
12. Martinez-Manez R, Sancenón F. 2003 Fluorogenic and chromogenic chemosensors and reagents for anions. *Chem. Rev.* **103**, 4419–4476. (doi:10.1021/cr010421e)
13. Schazmann B, Alhashimy N, Diamond D. 2006 Chloride selective calix[4] arene optical sensor combining urea functionality with pyrene excimer transduction. *J. Am. Chem. Soc.* **128**, 8607–8614. (doi:10.1021/ja061917m)
14. Kim H, Park J, Park I, Jin K, Jerng SE, Kim SH, Nam KT, Kang K. 2015 Coordination tuning of cobalt phosphates towards efficient water oxidation catalyst. *Nat. Commun.* **6**, 8253. (doi:10.1038/ncomms9253)
15. Bierlein JD, Vanherzeele H. 1989 Potassium titanyl phosphate: properties and new applications. *J. Optic. Soc. B* **6**, 622–633. (doi:10.1364/josab.6.000622)
16. Risk WP, Gosnell TR, Nurmikko AV. 2003 *Compact blue-green lasers*. Cambridge, UK: Cambridge University Press.
17. Hansia P, Guruprasad N, Vishveshwara S. 2006 Ab initio studies on the tri- and diphosphate fragments of adenosine triphosphate. *Biophys. Chem.* **119**, 127–136. (doi:10.1016/j.bpc.2005.07.011)
18. Rivas M, Casanovas J, del Valle LJ, Bertran O, Revilla-López G, Turon P, Puiggalí, J., Alemán C. 2015 An experimental-computer modeling study of inorganic phosphates surface adsorption on hydroxyapatite particles. *Dalton Trans.* **44**, 9980–9991. (doi:10.1039/c5dt00209)
19. Witko M, Tokarz R, Haber J, Hermann K. 2001 Electronic structure of vanadyl pyrophosphate: cluster model studies. *J. Mol. Catal. A: Chem.* **166**, 59–72. (doi:10.1016/s1381-1169(00)00470-2)
20. Ching W, Xu Y-N. 1991 Band structure and linear optical properties of $KTiOPO_4$. *Phys. Rev. B* **44**, 5332. (doi:10.1103/physrevb.44.5332)
21. Ching W, Rulis P. 2008 Large differences in the electronic structure and spectroscopic properties of three phases of $AlPO_4$ from *ab initio* calculations. *Phys. Rev. B* **77**, 125116. (doi:10.1103/physrevb.77.125116)
22. Liang L, Rulis P, Ching W. 2010 Mechanical properties, electronic structure and bonding of α-and β-tricalcium phosphates with surface characterization. *Acta Biomater.* **6**, 3763–3771. (doi:10.1016/j.actbio.2010.03.033)
23. Rulis P, Ouyang L, Ching W. 2004 Electronic structure and bonding in calcium apatite crystals: Hydroxyapatite, fluorapatite, chlorapatite, and bromapatite. *Phys. Rev. B* **70**, 155104. (doi:10.1103/physrevb.70.155104)
24. Rulis P, Yao H, Ouyang L, Ching W. 2007 Electronic structure, bonding, charge distribution, and x-ray absorption spectra of the (001) surfaces of fluorapatite and hydroxyapatite from first principles. *Phys. Rev. B* **76**, 245410. (doi:10.1103/physrevb.76.245410)
25. Misra A, Ching W. 2013 Theoretical nonlinear response of complex single crystal under multi-axial tensile loading. *Sci. Rep.* **3**, 1488. (doi:10.1038/srep01488)
26. Xu Y-N, Chung S-Y, Bloking JT, Chiang Y-M, Ching W. 2004 Electronic structure and electrical conductivity of undoped $LiFePO_4$. *Electrochem. Solid-State Lett.* **7**, A131–A134. (doi:10.1149/1.1703470)
27. Xu Y-N, Ching W, Chiang Y-M. 2004 Comparative studies of the electronic structure of $LiFePO_4$, $FePO_4$, Li_3PO_4, $LiMnPO_4$, $LiCoPO_4$, and $LiNiPO_4$. *J. Appl. Phys.* **95**, 6583–6585. (doi:10.1063/1.1667422)
28. Poudel L, Rulis P, Liang L, Ching W. 2014 Electronic structure, stacking energy, partial charge, and hydrogen bonding in four periodic B-DNA models. *Phys. Rev. E* **90**, 022705. (doi:10.1103/PhysRevE.90.022705)
29. Schimelman JB *et al.* 2015 Optical properties and electronic transitions of DNA oligonucleotides as a function of composition and stacking sequence. *Phys. Chem. Chem. Phys.* **17**, 4589–4599. (doi:10.1039/c4cp03395g)
30. Poudel L, Wen AM, French RH, Parsegian VA, Podgornik R, Steinmetz NF, Ching WY. 2015 Electronic structure and partial charge distribution of doxorubicin in different molecular environments. *Chemphyschem.* **16**, 1451–1460. (doi:10.1002/cphc.201402893)
31. Poudel L, Steinmetz NF, French RH, Parsegian VA, Podgornik R, Ching W-Y. 2016 Implication of the solvent effect, metal ions and topology in the electronic structure and hydrogen bonding of human telomeric G-quadruplex DNA. *Phys. Chem. Chem. Phys.* **18**, 21 573–21 585. (doi:10.1039/c6cp04357g)
32. Poudel L, Twarock R, Steinmetz NF, Podgornik R, Ching W-Y. 2017 Impact of hydrogen bonding in binding site between capsid protein and MS2 bacteriophage ssRNA. *J. Phys. Chem. B* **121**, 6321–6330. (doi:10.1021/acs.jpcb.7b02569)
33. Harcharras M, Capitelli F, Ennaciri A, Brouzi K, Moliterni A, Mattei G, Bertolasi V. 2003 Synthesis, X-ray crystal structure and vibrational spectroscopy of the acidic pyrophosphate $KMg_{0.5}H_2P_2O_7 \cdot H_2O$. *J. Solid State Chem.* **176**, 27–32. (doi:10.1016/s0022-4596(03)00339-6)
34. Altomare A, Burla MC, Camalli M, Cascarano GL, Giacovazzo C, Guagliardi A, Moliterni AG, Polidori G, Spagna R. 1999 SIR97: a new tool for crystal structure determination and refinement. *J. Appl. Crystallogr.* **32**, 115–119. (doi:10.1107/s0021889898007717)

35. Sheldrick G. 1997 *SHELXL-97: crystal structure refinement program*. Göttingen, Germany: University of Göttingen.
36. Kresse G, Furthmüller J. 2001 Vienna Ab-initio Simulation Package (VASP). Vienna, Austria: Vienna University.
37. Perdew JP, Burke K, Ernzerhof M. 1996 Generalized gradient approximation made simple. *Phys. Rev. Lett.* **77**, 3865. (doi:10.1103/physrevlett.77.3865)
38. Monkhorst HJ, Pack JD. 1976 Special points for Brillouin-zone integrations. *Phys. Rev. B* **13**, 5188–5192. (doi:10.1103/physrevb.13.5188)
39. Ching W-Y, Rulis P. 2012 *Electronic structure methods for complex materials: the orthogonalized linear combination of atomic orbitals*. Oxford, UK: Oxford University Press.
40. Li N, Ching W-Y. 2014 Structural, electronic and optical properties of a large random network model of amorphous SiO_2 glass. *J. Non-Cryst. Solids* **383**, 28–32. (doi:10.1016/j.jnoncrysol.2013.04.049)
41. Li N, Sakidja R, Aryal S, Ching W-Y. 2014 Densification of a continuous random network model of amorphous SiO_2 glass. *Phys. Chem. Chem. Phys.* **16**, 1500–1514. (doi:10.1039/c3cp53192a)
42. Walker B, Dharmawardhana CC, Dari N, Rulis P, Ching W-Y. 2015 Electronic structure and optical properties of amorphous GeO_2 in comparison to amorphous SiO_2. *J. Non-Cryst. Solids* **428**, 176–183. (doi:10.1016/j.jnoncrysol.2015.08.018)
43. Baral K, Adhikari P, Ching WY. 2016 *Ab initio* modeling of the electronic structures and physical properties of a-$Si_{1-x}Ge_xO_2$ glass (x= 0 to 1). *J. Am. Ceram. Soc.* **99**, 3677–3684. (doi:10.1111/jace.14386)
44. Baral K, Ching WY. 2017 Electronic structures and physical properties of Na_2O doped silicate glass. *J. Appl. Phys.* **121**, 245103. (doi:10.1063/1.4987033)
45. Mulliken RS. 1955 Electronic population analysis on LCAO—MO molecular wave functions. I. *J. Chem. Phys.* **23**, 1833–1840. (doi:10.1063/1.1740588)
46. Mulliken R. 1955 Electronic population analysis on LCAO—MO molecular wave functions. II. Overlap populations, bond orders, and covalent bond energies. *J. Chem. Phys.* **23**, 1841–1846. (doi:10.1063/1.1740589)
47. Dharmawardhana C, Misra A, Ching W-Y. 2014 Quantum mechanical metric for internal cohesion in cement crystals. *Sci. Rep.* **4**, Article number 7332. (doi:10.1038/srep07332)
48. Martin PC. 1967 Sum rules, Kramers-Kronig relations, and transport coefficients in charged systems. *Phys. Rev.* **161**, 143–155. (doi:10.1103/physrev.161.143)
49. Nielsen O, Martin RM. 1983 First-principles calculation of stress. *Phys. Rev. Lett.* **50**, 697–700. (doi:10.1103/physrevlett.50.697)
50. Yao H, Ouyang L, Ching WY. 2007 *Ab initio* calculation of elastic constants of ceramic crystals. *J. Am. Ceram. Soc.* **90**, 3194–3204. (doi:10.1111/j.1551-2916.2007.01931.x)
51. Reuss A. 1929 Berechnung der fließgrenze von mischkristallen auf grund der plastizitätsbedingung für einkristalle. *ZAMM.* **9**, 49–58. (doi:10.1002/zamm.19290090104)
52. Hill R. 1952 The elastic behaviour of a crystalline aggregate. *Proc. Phys. Soc. A* **65**, 349–354. (doi:10.1088/0370-1298/65/5/307)
53. Aryal S, Sakidja R, Ouyang L, Ching W-Y. 2015 Elastic and electronic properties of Ti_2Al (C_xN_{1-x}) solid solutions. *J. Eur. Ceram. Soc.* **35**, 3219–3227. (doi:10.1016/j.jeurceramsoc.2015.03.023)
54. Aryal S, Matsunaga K, Ching W-Y. 2015 Ab initio simulation of elastic and mechanical properties of Zn-and Mg-doped hydroxyapatite (HAP). *J. Mech. Behav. Biomed. Mater.* **47**, 135–146. (doi:10.1016/j.jmbbm.2015.03.018)
55. Dharmawardhana C, Bakare M, Misra A, Ching WY. 2016 Nature of interatomic bonding in controlling the mechanical properties of calcium silicate hydrates. *J. Am. Ceram. Soc.* **99**, 2120–2130. (doi:10.1111/jace.14214)
56. Adhikari P, Xiong M, Li N, Zhao X, Rulis P, Ching W-Y. 2016 Structure and electronic properties of a continuous random network model of an amorphous Zeolitic Imidazolate Framework (a-ZIF). *J. Phys. Chem. C* **120**, 15 362–15 368. (doi:10.1021/acs.jpcc.6b0633)
57. Adhikari P, Dharmawardhana C, Ching W-Y. 2017 Structural properties of hydrogrossular mineral series. *J. Am. Ceram. Soc.* **100**, 4317–4330. (doi:10.1111/jace.14970)
58. Ching W, Rulis P, Misra A. 2009 Ab initio elastic properties and tensile strength of crystalline hydroxyapatite. *Acta Biomater.* **5**, 3067–3075. (doi:10.1016/j.actbio.2009.04.030)
59. Togo A, Tanaka I. 2015 First principles phonon calculations in materials science. *Scr. Mater.* **108**, 1–5. (doi:10.1016/j.scriptamat.2015.07.021)
60. Khaoulaf R, Ennaciri A, Ezzaafrani M, Capitelli F. 2013 Structure and vibrational spectra of a new acidic diphosphate $K_2Cu\ (H_2P_2O7)_2{\cdot}2H_2O$. *Phosphorus, Sulfur, Silicon* **188**, 1038–1052. (doi:10.1080/10426507.2012.736096)
61. Capitelli F, Khaoulaf R, Harcharras M, Ennaciri A, Habyby SH, Valentini V, Mattei G, Bertolasi V. 2005 Crystal structure and vibrational spectroscopy of the new acidic diphosphate $(NH_4)_2Zn(H_2P_2O_7)_2 \cdot 2H_2O$. *Zeitschrift für Kristallographie-Cryst. Mat.* **220**, 25–30. (doi:10.1524/zkri.220.1.25.58883)
62. Brouzi K, Ennaciri A, Capitelli F, Valentini V, Mattei G, Harcharras M. 2005 Vibrational study of manganese ammonium dihydrogendiphosphate hydrated MnO. $5NH_4H_2P_2O_7 \cdot H_2O$. *Phosphorus, Sulfur, Silicon*. **180**, 545–553. (doi:10.1080/10426509051730 7)
63. Khaoulaf R, Ezzaafrani M, Ennaciri A, Harcharras M, Capitelli F. 2012 Vibrational study of dipotassium zinc bis (dihydrogendiphosphate) dihydrate, $K_2ZN\ (H_2P_2O_7)_2 \cdot 2H_2O$. *Phosphorus, Sulfur, Silicon* **187**, 1367–1376. (doi:10.1080/10426507.2012.685669)